INTERNATIONAL JOURNAL FOR NUMERICAL METHODS IN FLUIDS, VOL. 10, 875–888 (1990)

AN APPLICATION OF THE VORTICITY–VECTOR POTENTIAL METHOD TO LAMINAR CUBE FLOW

ROBIN RAUL, PETER S. BERNARD AND FRANK T. BUCKLEY, JR.
Department of Mechanical Engineering, The University of Maryland, College Park, MD 20742, U.S.A.

SUMMARY

Three-dimensional incompressible laminar flow around a cube is investigated using the vorticity–vector potential formulation of the equations of motion. Numerical solutions to a semi-implicit finite difference approximation to the vorticity transport equation coupled to discrete Poisson equations for the scalar and vector potentials are obtained using an eight-colour SOR algorithm. Calculations are done at a range of Reynolds numbers from 10 to 100. The predicted drag and other flow characteristics are found to agree well with experimental results, including those from a cube drop experiment performed for the present study.

KEY WORDS 3D Incompressible laminar flow Cube Vorticity–vector potential formulation Finite difference Vorticity transport equation Poisson equations SOR algorithm

1. INTRODUCTION

Numerical schemes for computing three-dimensional flow fields have largely been based upon the primitive variable formulation of the Navier–Stokes equation. In contrast, two-dimensional flows are quite commonly calculated using vorticity–streamfunction methods. To some extent this turnabout is a result of the additional storage requirements and lingering conceptual problems concerning boundary conditions which are associated with the three-dimensional analogue of the streamfunction, namely the vector potential. These limitations have often appeared to outweigh the potential benefits accruing from the use of the vector potential, which include the exact satisfaction of the continuity condition and elimination of the computational effort needed to accurately compute the pressure field at each time step. The advent of supercomputers, with their large fast memories, however, has made storage limitations less critical so that the development of vector potential methods with improved boundary conditions has become the object of much recent interest.[1–3]

In some circumstances the use of the vorticity as the dependent variable is highly desirable or even essential as, for example, in the calculation of turbulent flows using a vorticity-based turbulence closure scheme.[4, 5] In this case a primitive variable approach is impractical since the implementation of the vorticity closure technique in this context requires overcoming many, as yet unsolved, technical problems.

The vorticity–vector potential approach has been the subject of much investigation since Aziz and Hellums[6] showed that it can lead to relatively fast and stable simulations of three-dimensional flows. Hirasaki and Hellums[7] formally derived a set of consistent boundary conditions for the vector potential which, while practical in the case of confined flows, were too complex for use in problems with flowthrough, as in a duct. Later Hirasaki and Hellums[8] and Richardson and

0271–2091/90/080875–14$07.00 *Received 1 June 1988*

Cornish[9] added a scalar potential to the formulation and showed that the boundary conditions on the vector potential could be greatly simplified in this case. Wong and Reizes[1] claimed that inclusion of a scalar potential can in fact destroy a major advantage inherent in the vector potential, which is to assure local and global continuity. Later Tutty,[2] contradicting Wong and Reizes, argued that the use of a scalar potential does not interfere with the satisfaction of continuity, though it can lead to difficulties at sharp corners, where the scalar potential boundary condition is discontinuous.

In recent years the vorticity–vector potential approach has been used to study a variety of three-dimensional flow fields. Among these, Wu *et al.*[10] studied unsteady problems, Wong and Reizes[11] applied it to three-dimensional multiply connected regions, Morino[12] extended the method to compressible viscous unsteady flows and Yang and Camarero[13] considered duct flows. Improvements in computational efficiency resulting from a new set of boundary conditions for the vector potential have also been reported for the case of annular flows.[3]

In the present paper, computations of the three-dimensional laminar incompressible uniform flow around a cube are described. The vorticity–vector potential formulation given by Richardson and Cornish[9] is followed. Calculations are done at Reynolds numbers between 10 and 100. The importance of such bluff body flows is evident in many fields, such as automotive aerodynamic design and the prediction of wind forces on tall structures. Computation of cube flow in the more realistic case of high Reynolds numbers, when turbulence is present, will be the next step in the current research programme.

The numerical scheme which is used consists of a fully vectorizable eight-colour SOR algorithm. This is employed to solve the four discrete Poisson equations for scalar and vector potentials plus semi-implicit finite difference approximations to the three vorticity equations. The computed drag compares well with related experimental data, including the results of a cube drop experiment which were done in support of the present study. Other characteristics of the solution appear to be in agreement with similar bluff body flow fields.

The next section contains a brief description of the present flow field as well as the appropriate governing equations. In Section 3 some computational details of the numerical scheme including the treatment of boundary conditions are presented, while Section 4 discusses the drag data obtained from the cube drop experiments. Finally, Section 5 contains numerical results followed by Section 6 in which conclusions are given.

2. FORMULATION

The flow field considered here is shown in Figure 1. The computational domain is a rectangular parallelepiped region surrounding a cube situated at its centre, in which x is the streamwise direction and y and z are spanwise directions. Lengths are scaled by the cube diameter. The boundaries of the flow domain are assumed to be in the far field of the cube flow. The dimensionless lengths of the computational domain are L_x, L_y and L_z. For most calculations these lengths were given a magnitude of 10 cube diameters, a distance which appeared to be, after some testing, large enough so that the solutions were for the most part independent of them. Generally, the inherent symmetries of the cube flow field were utilized so that just a quarter-domain solution was obtained. This allowed for better grid resolution and wider far field boundaries. Some calculations were also performed using a mesh covering the whole domain as well. These served both as a check on the quarter-domain calculations and as preparation for later studies of non-symmetrical cases.

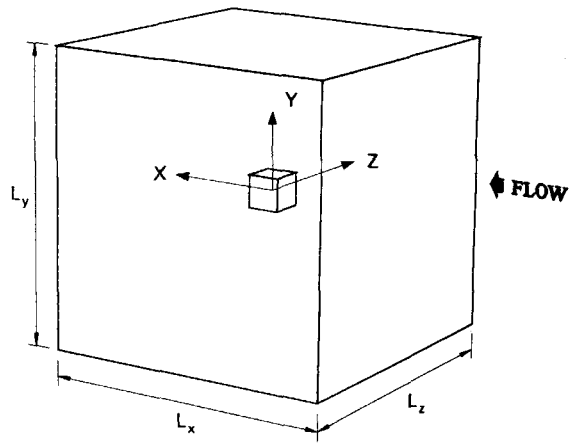

Figure 1. Computational domain

The vorticity transport and continuity equations in three-dimensional laminar incompressible flow are respectively

$$\frac{\partial \mathbf{w}}{\partial t} + (\mathbf{u}\cdot\nabla)\mathbf{w} - (\mathbf{w}\cdot\nabla)\mathbf{u} = \left(\frac{1}{Re}\right)\nabla^2\mathbf{w}, \tag{1}$$

$$\nabla\cdot\mathbf{u} = 0, \tag{2}$$

where

$$\mathbf{w} = \nabla\times\mathbf{u} \tag{3}$$

is the vorticity vector, $\mathbf{u}=(u, v, w)$ is the velocity vector and Re is the Reynolds number based on cube diameter and free stream velocity U_∞. Introducing a vector potential $\boldsymbol{\Psi}$ and a scalar potential ϕ, $\mathbf{u}$ may be written as

$$\mathbf{u} = \nabla\phi + \nabla\times\boldsymbol{\Psi}. \tag{4}$$

Since $\nabla\cdot(\nabla\times\boldsymbol{\Psi})\equiv 0$, substitution of equation (4) into equation (2) gives

$$\nabla^2\phi = 0. \tag{5}$$

A relation between $\boldsymbol{\Psi}$ and $\mathbf{w}$ is obtained by taking the curl of equation (4), which yields

$$\nabla(\nabla\cdot\boldsymbol{\Psi}) - \nabla^2\boldsymbol{\Psi} = \mathbf{w}.$$

Since the decomposition (4) is not unique, for convenience $\boldsymbol{\Psi}$ can be chosen to be solenoidal, i.e.

$$\nabla\cdot\boldsymbol{\Psi} = 0,$$

and hence

$$\nabla^2\boldsymbol{\Psi} = -\mathbf{w}. \tag{6}$$

Equations (1) and (4)–(6) are sufficient to determine the complete cube flow field once the appropriate boundary conditions are specified.

Consistent with References 8 and 9, the boundary conditions for the present calculation may be taken as the following. For ϕ, the condition

$$\partial\phi/\partial n = \hat{\mathbf{n}}\cdot\mathbf{u} \tag{7}$$

must be satisfied on all boundaries. Here $\hat{\mathbf{n}}$ is the outward drawn unit normal. On the cube surfaces equation (7) reduces to $\partial\phi/\partial n=0$ in view of the non-penetration condition. On the outer boundaries $\mathbf{u}$ is not known *a priori*, but it may be approximated using

$$\mathbf{u}_s=\nabla\phi_s, \tag{8}$$

where

$$\phi_s(x, y, z)=U_\infty\left(1+\frac{a_s^3}{2(x^2+y^2+z^2)^{3/2}}\right)x \tag{9}$$

is the potential field due to a sphere of volume equal to that of the cube, a_s is the sphere diameter and U_∞ is the upstream velocity. In the distant far field as $L_x, L_y, L_z\to\infty$, $\mathbf{u}$ and $\mathbf{u}_s$ become equal.[14]

The vector potential satisfies the conditions

$$\psi_{t_1}=\psi_{t_2}=\partial\psi_n/\partial n=0 \tag{10}$$

on solid surfaces, where the subscripts 't' and 'n' denote tangential and normal components respectively. Since the flow is assumed to be fully developed on the outer boundaries, the soft boundary condition[13]

$$\partial^2\psi_i/\partial n^2=0,$$

where $i=1, 2, 3$, was used at these locations.

On the cube boundaries $\mathbf{w}$ was obtained directly from its definition, so that, for example, on the cube face normal to $+y$,

$$\omega_1=\partial w/\partial y, \qquad \omega_2=0, \qquad \omega_3=-\partial u/\partial y.$$

Here ω_1, ω_2 and ω_3 are the scalar components of $\mathbf{w}$. On the outer boundaries the vorticity derivatives appearing in equation (1) were approximated using one-sided differences so as to obviate the need for $\mathbf{w}$ boundary conditions in these locations. For the calculations performed in the quarter domain, the appropriate symmetry and antisymmetry boundary conditions on ϕ, $\boldsymbol{\Psi}$ and $\mathbf{w}$ were incorporated at the symmetry planes of the reduced domain.

Prediction of the total drag on the cube, which contains viscous or skin friction drag and pressure drag components, depends on a knowledge of the shear stresses and pressure distribution over the cube surfaces. The shear stresses, which contribute to viscous drag, are directly proportional to the local tangential vorticity components on each surface of the cube. Thus, for example, on the surface with $+y$ normal the viscous drag is given by

$$D_y=\mu\int_{-1/2}^{+1/2}\int_{-1/2}^{+1/2}\omega_3\,\mathrm{d}x\mathrm{d}z. \tag{11}$$

Expressions such as this were evaluated using the two-dimensional trapazoidal rule.[15]

The pressure P may be obtained as the solution to the Poisson equation

$$\nabla^2P-\nabla\cdot(\mathbf{u}\times\mathbf{w})=0, \tag{12}$$

which follows by taking the divergence of the Navier–Stokes equation. Neumann-type boundary conditions for P may be derived at the cube surfaces from the momentum equation. For example, at the surface with normal in the $+y$-direction,

$$\frac{\partial P}{\partial y}=\frac{1}{Re}\left(\frac{\partial^2 v}{\partial y^2}\right). \tag{13}$$

At the outer boundaries soft conditions were applied, i.e. the second derivatives of P in the outward normal direction were set to zero.

3. COMPUTATIONAL SCHEME

Figure 2 shows the finite difference mesh used in the quarter-domain calculation. The quarter of the cube which is indicated occupies the region $-0{\cdot}5 \leqslant x \leqslant 0{\cdot}5$, $-0{\cdot}5 \leqslant y, z \leqslant 0$. The physical co-ordinate mesh was transformed to a uniform grid in a curvilinear co-ordinate system s_1, s_2, s_3. In each co-ordinate direction an orthogonal mapping of the general form

$$x(s) = \begin{cases} s\gamma + (0{\cdot}5 - \gamma)[\frac{15}{8}s - \frac{5}{4}s^3 + \frac{3}{8}s^5], & |x_i| \leqslant 0{\cdot}5, \\ 0{\cdot}5 + \gamma(s-1)e^{A(s-1)^M}, & |x_i| \geqslant 0{\cdot}5 \end{cases} \tag{14}$$

was used. Here $\gamma = h N_c/(N_a - 1)$ and

$$A = \ln\left(\frac{L - 0{\cdot}5}{\gamma(N/N_c - 1)}\right) \Big/ \left(\frac{N}{N_c} - 1\right)^M,$$

where N is the total number of grid points in the particular direction, L is the extent of the computational domain, N_a is the grid point of the lower cube surface, $2N_c$ is the number of grid points spanning the cube and h and M are adjustable parameters controlling the density of the placement of mesh points. The two functions in equation (14) are continuous through second derivatives at the point where they meet at the cube boundary. Nominal values of the grid parameters used in this study were $N_x = 69$, $N_y = 35$, $N_z = 35$, $N_a = 27$, $N_c = 17$, $M = 2$ and $h = 0{\cdot}2$. Some variations in these quantities were made to test the grid sensitivity of the computed solutions, which was found to be within acceptable limits.

Numerical solutions to the cube flow field were obtained by solving finite difference approximations to equations (1), (4)–(6) and (12) transformed into the s_i co-ordinate system. Second-order spatial differencing was incorporated throughout. Central differencing was used in the interior and one-sided differencing at the boundaries. Note that the forcing term in equation (12) is effectively first-order accurate since it depends on derived quantities. For the vorticity equation, a first-order semi-implicit time discretization was employed. For a complete discussion of the computational scheme and differenced form of the transformed equations, see Reference 16.

The implicit finite difference equations were solved iteratively on the three-dimensional mesh using an eight-colour SOR algorithm. In this approach, eight sweeps through the mesh are

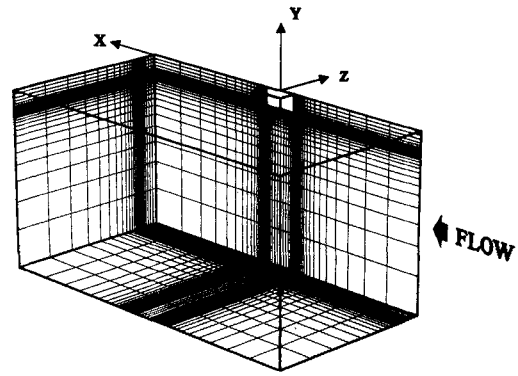

Figure 2. Grid in quarter domain

performed, updating just every other nodal value in the three directions. The starting point for each of the passes through the mesh varies in turn over the eight nodes of the grid box with corners (i, j, k), $1 \leqslant i, j, k \leqslant 2$. This algorithm allows for full vectorization in that the mesh points updated in each sweep are non-adjacent so they may be relaxed in parallel. The relaxation factors used in solving the equations for ϕ, Ψ, $\mathbf{w}$ and P were 1·04, 1·7, 1·0 and 1·8 respectively. Equation (5) was solved at the inception of the calculations and the result stored for subsequent use.

In the Reynolds number range considered here, no evidence of vortex shedding was observed. Consequently, the numerical solutions were marched forward in time until a steady state condition was reached. At each time step the discrete equations were solved using a convergence criteria in which the global L_2 norm

$$\| f^{l+1,n} - f^{l,n} \|_2 \equiv \left(\sum_{i,j,k} (f^{l+1,n}_{i,j,k} - f^{l,n}_{i,j,k})^2 \right)^{1/2} < 10^{-5}.$$

Here f represents any of the variables ϕ, Ψ, $\mathbf{w}$ or P, l denotes the iteration step in the SOR algorithm, n is the time step and the summation is over the three-dimensional mesh. Convergence to a steady solution was considered accomplished when $\|\mathbf{w}^{n+1} - \mathbf{w}^n\|_2 < 10^{-5}$.

The implementation of the boundary conditions on the sharp edges and corners of the cube required special consideration. To avoid a singularity in the normal direction at the cube surface, it was assumed that the cube, however well machined, would have a finite radius at the edges and corners. In accordance with this concept, the boundary condition on ϕ at an edge like that in Figure 3(a) was taken as

$$\frac{\phi_{i+1,j+1,k} - \phi_{i,j,k}}{\Delta n} = 0,$$

while at a corner as in Figure 3(b) it becomes

$$\frac{\phi_{i+1,j+1,k+1} - \phi_{i,j,k}}{\Delta n} = 0.$$

At the edge shown in Figure 3(a) unit vectors in the normal and tangential directions are given by

$$\hat{\mathbf{n}} = (\hat{\mathbf{i}} + \hat{\mathbf{j}}) \frac{1}{\sqrt{2}}, \qquad \hat{\mathbf{t}}_1 = (\hat{\mathbf{i}} - \hat{\mathbf{j}}) \frac{1}{\sqrt{2}}, \qquad \hat{\mathbf{t}}_2 = \hat{\mathbf{k}}.$$

The boundary condition on the tangential components of Ψ was implemented by setting

$$\Psi \cdot \hat{\mathbf{t}}_1 = (\psi_1 - \psi_2) = 0 \tag{15}$$

and

$$\Psi \cdot \hat{\mathbf{t}}_2 = \psi_3 = 0. \tag{16}$$

For the normal component

$$\psi_n = \Psi \cdot \hat{\mathbf{n}} = (\psi_1 + \psi_2) \frac{1}{\sqrt{2}},$$

the condition

$$\frac{\partial \psi_n}{\partial n} = \hat{\mathbf{n}} \cdot \nabla \psi_n = 0$$

implies that

$$\frac{\partial}{\partial x}(\psi_1 + \psi_2) + \frac{\partial}{\partial y}(\psi_1 + \psi_2) = 0.$$

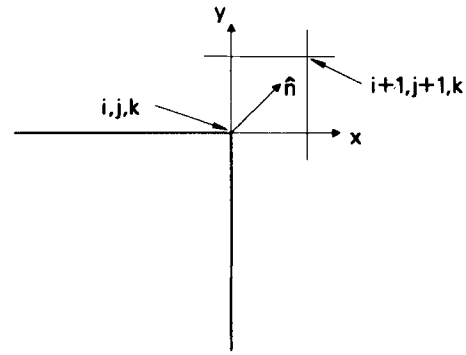

Figure 3(a). Edge differencing

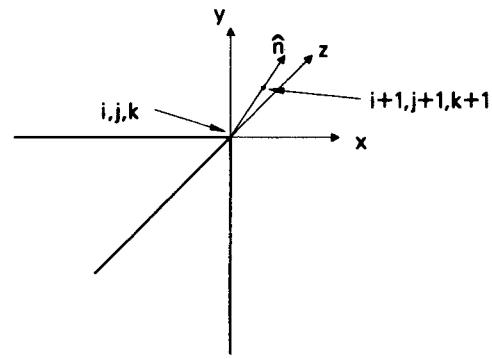

Figure 3(b). Corner differencing

After replacing the derivatives in this expression with forward differences, using equation (15) and assuming $\Delta x = \Delta y$, it follows that

$$\psi_{1_{i,j,k}} = \psi_{2_{i,j,k}} = \tfrac{1}{4}[(\psi_1 + \psi_2)_{i+1,j,k} + (\psi_1 + \psi_2)_{i,j+1,k}]. \tag{17}$$

A similar analysis applied to a corner such as that depicted in Figure 3(b) yields the following result:

$$\psi_{1_{i,j,k}} = \psi_{2_{i,j,k}} = \psi_{3_{i,j,k}} = \tfrac{1}{9}[(\psi_1 + \psi_2 + \psi_3)_{i+1,j,k} + (\psi_1 + \psi_2 + \psi_3)_{i,j+1,k} + (\psi_1 + \psi_2 + \psi_3)_{i,j,k+1}].$$

Boundary conditions for the remaining edges and corners can be derived by generalizing this argument.

Several other formulations of boundary conditions on the corners and edges of the cube were examined, including one in which these points were assumed to be in the interior of the flow. While all the approaches led to similar gross characteristics of the computed flow field, the current one appears to give substantially better drag predictions than the others. The formulae given here also did not appear to produce the numerical errors at the corners which were cited in Reference 2.

4. EXPERIMENTAL RESULTS

An extensive literature survey was unable to locate experimental data concerning the laminar flow around a cube in free uniform flow. Hence, to aid in verifying the numerical calculations, an experiment was designed to obtain the drag coefficient of a cube in laminar flow at a range of low

Reynolds numbers. This consisted of dropping a series of cubes of various diameters a and weights W in a tank of glycerine of density ρ_g. After determining the cubes had reached terminal speed u_t, the drag coefficient C_D was computed from the relation

$$C_D = \frac{W - a^3 \rho_g}{1/2 \rho_g u_t^2}, \tag{18}$$

which expresses the balance of forces acting on the cube.

For the experiment a glass tank of diameter $d = 8''$ and height 4′ was used. The tank was filled with glycerine whose kinematic viscosity was measured independently using a capillary viscometer. Plexiglass cubes of various dimensions were constructed with a slice of aluminium at one end so as to enhance their stability during the fall. The cube weights were varied through the addition of small weights to a cylindrical cavity drilled in the top of the cube. In this way a large range of Reynolds numbers could be generated. In order to eliminate wall effects, the experiment was repeated for several different cube sizes with the results then extrapolated to the case where the walls are at infinity. Cubes of dimension 1·0″, 1·5″, 2·0″, 2·5″ and 3·0″ were used. The Reynolds number versus C_D was plotted for the five cases on a log–log scale. A separate plot of C_D versus a/d was then constructed for a set of given Reynolds numbers. In order to extrapolate the results to $a/d = 0$, an equation was fitted through these data points. A best fit was found to occur for the relation

$$\ln(C_D) = 1{\cdot}7 + 19{\cdot}8(a/d)^3,$$

where it is assumed that as $a/d \to 0$ the slope of these curves approaches zero. The extrapolated data were subsequently used to test the accuracy of the computed solutions. This will be described in the next section.

5. NUMERICAL RESULTS

Calculations were performed on the San Diego Supercomputer Center (SDSC) CRAY X-MP/48 whose four CPUs provide a theoretical peak speed of 840 Mflops (millions of floating-point operations per second). Approximately two million words of fast memory is available to users. In view of the large number of arrays necessary to store for the present numerical scheme, the largest grid which could be accommodated was limited to approximately 100 000 nodes. The typical mesh used in the study, which had $69 \times 35 \times 35 = 84\,525$ grid points covering the quarter domain, was close to this limit.

The SOR relaxation in the case of $\mathbf{w}$ required approximately 10 iterations for $\|\mathbf{w}^{l+1,n} - \mathbf{w}^{l,n}\|_2 < 10^{-5}$, while $\boldsymbol{\Psi}$ converged in about 20 iterations. These values reduced to 1 as the overall convergence of $\mathbf{w}$ progressed. Approximately 1500 time steps were sufficient for convergence in the $\mathbf{w}$ field. For the calculation of ϕ and P, on the order of 1000 iterations were needed for convergence. With good initial conditions this number could be reduced substantially.

Calculations were done for $Re = 10$, 20, 30, 40, 60, 80 and 100. It took typically about 10 min of CPU time to get solutions for ϕ and about 2 h of CPU time to get complete solutions. Since many of the Re cases were started from previously converged solutions obtained at lower Re, significantly less time was needed for these calculations.

Comparison of the calculated drag with the cube drop experiment is shown in Figure 4. To cover the Reynolds number range above 20, for which data from other experiments or calculations could not be found, the equivalent drag data for square plates held normal to the flow[17] is given. Presumably, the trend in this data, except at the lowest Reynolds numbers, should have some relevance to the cube flow field. It is evident that the calculations compare well with the

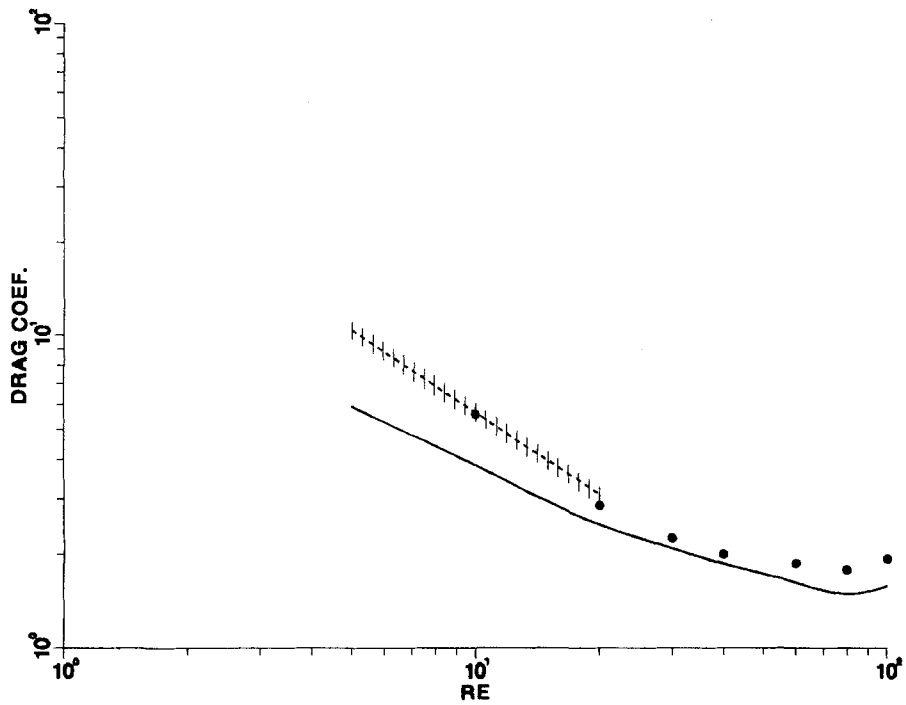

Figure 4. Computed and experimental drag versus *Re*: ●, calculations; – – –, cube drop experiments; ——, plates

experimental results. The computed drag of the cube is a little higher than that of square plates, which is perhaps expected, since the added extra dimension of the three-dimensional cube gives a mechanism for higher viscous drag.

The calculated pressure and skin friction drag coefficients are plotted in Figure 5 as a function of *Re*. The trend conforms to the expected variation of these quantities with each other and with Reynolds number. In particular, at low *Re* there is little separation and the drag is mostly viscous. As *Re* is increased, separation of the flow becomes more pronounced, thus reducing viscous drag and increasing pressure drag.

It may be observed in Figure 5 that the computed pressure drag is somewhat underpredicted at the lowest values of *Re*. In fact, at $Re = 10$ it is slightly negative. These unphysical values appear to reflect the difficulty of computing the pressure in low-Reynolds-number external flows in a bounded computational domain.[18, 19] Any attempt to augment the size of the solution domain is countered by the need to maintain an adequate grid density at the cube surface. In particular, as $Re \rightarrow O(1)$, the calculated pressure depends increasingly on the accuracy of implementation of (13). Some attempt was made to increase the computational domain in the case of $Re = 10$. In these computations the viscous drag remained virtually unchanged, while the pressure drag increased towards zero. The result cited in Figure 5 used a mesh in which $N_x = 89$ and $L_x = 18$. Unfortunately, consideration of larger values of L_x was not possible since with $N_x = 89$ the storage limitation of the SDSC CRAY X-MP/48 was reached. Since the pressure calculation is done only after a converged solution for **u** and **w** is obtained, it appears that the use of the vector potential in low-*Re* flows has the inadvertent benefit of limiting the sensitivity of the computed solution to the effect of far field boundaries.

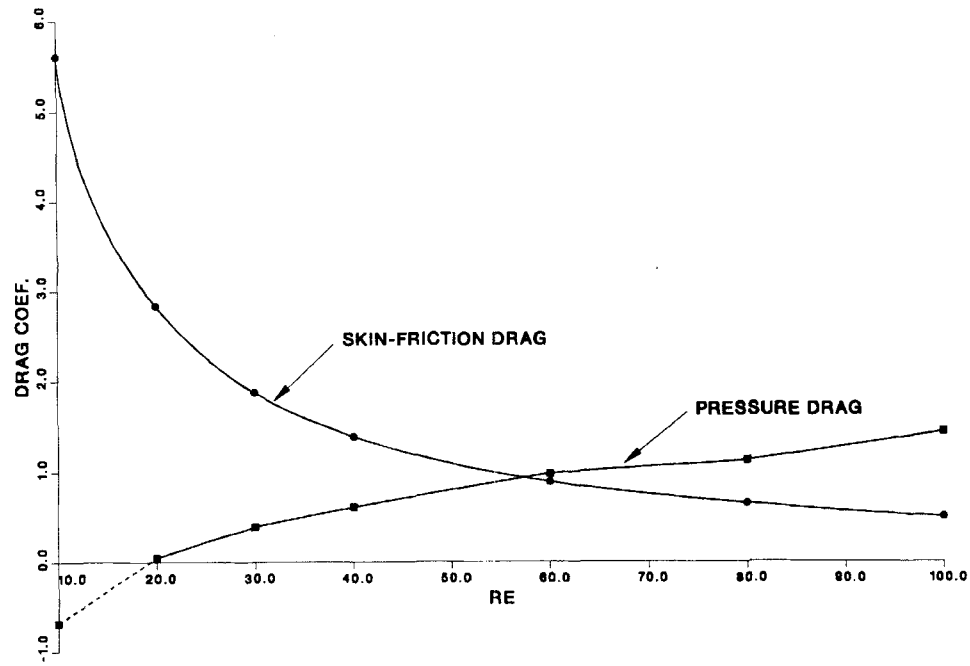

Figure 5. Computed skin friction and pressure drag versus *Re*

Figures 6(a) to 6(d) give plots of the projection of the velocity field on two-dimensional slices through the middle of the cube. For the sake of brevity, only some planes from some of the cases are shown. As expected, the relaxation toward the free stream velocity at the outer boundaries is visible. The flow in the rear of the cube shows a recirculation zone, whose size increases with Reynolds number. A measure of wake length may be defined as the distance to the rear cube surface from the point on the x-axis where the flow reverses. Figure 7 shows the variation of wake size with *Re*. Notice that this varies linearly at low *Re* numbers as is the case with spheres.[20] The absence of periodic shedding of vorticity in the present study is to be contrasted with the case of a sphere where the phenomenon commences at $Re \approx 40$. The difference is readily explained, however, by the presence of sharp edges in the cube geometry which strongly stabilize the location of the rear separation lines. It should be noted that periodic shedding was also not observed for several calculations performed on the full flow domain.

Contours of the spanwise vorticity ω_3 in the xy plane through the middle of the cube are shown in Figures 8(a) to 8(d). Again only some of the cases are shown. It is seen that the maximum vorticity is generated at the front edges and subsequently convects downstream, the extent of this region increasing for higher Reynolds numbers. A second local maximum in vorticity occurs at the rear edges due to the peaking velocity gradient as the flow navigates past the sharp rear of the body.

Figures 9(a) and 9(b) depict contours of the pressure coefficient on the cube surfaces. It is seen that there are large pressure gradients near all of the edges. The rear surface, being in the wake, contains a relatively large region of low pressure in a pattern which is strongly influenced by the presence of the corners. It is interesting to note that in both cases there is a region of low pressure coefficient on the side surfaces near the front edge, corresponding to an incipient recirculation zone which may be expected to develop at this location. The pressure patterns on the front and side also show evidence of slipping of the fluid stream around the sides of the cube corners.

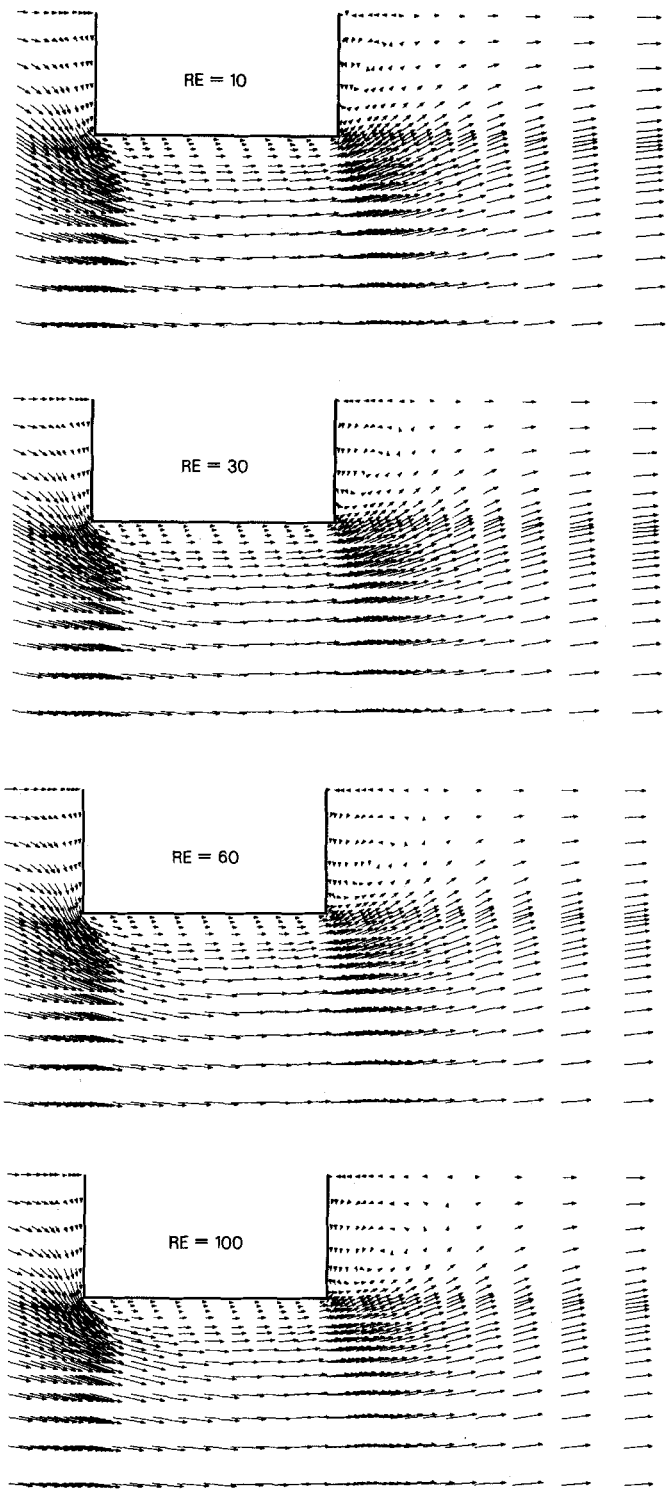

Figure 6. Velocity field in xy plane through middle of cube at Re=(a) 10, (b) 30, (c) 60 and (d) 100

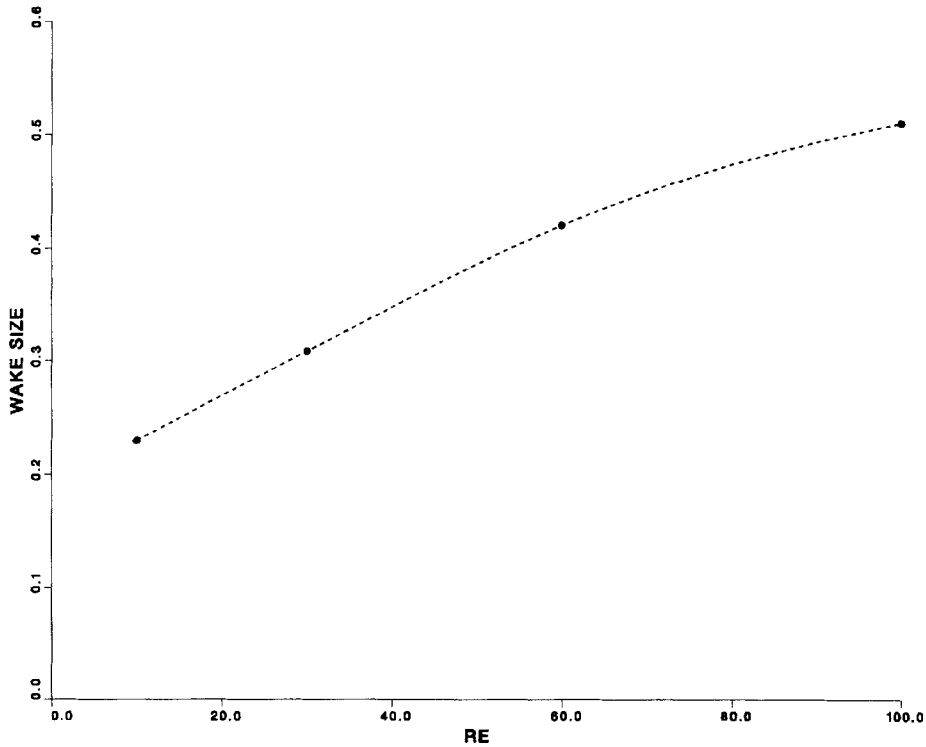

Figure 7. Wake size versus *Re*

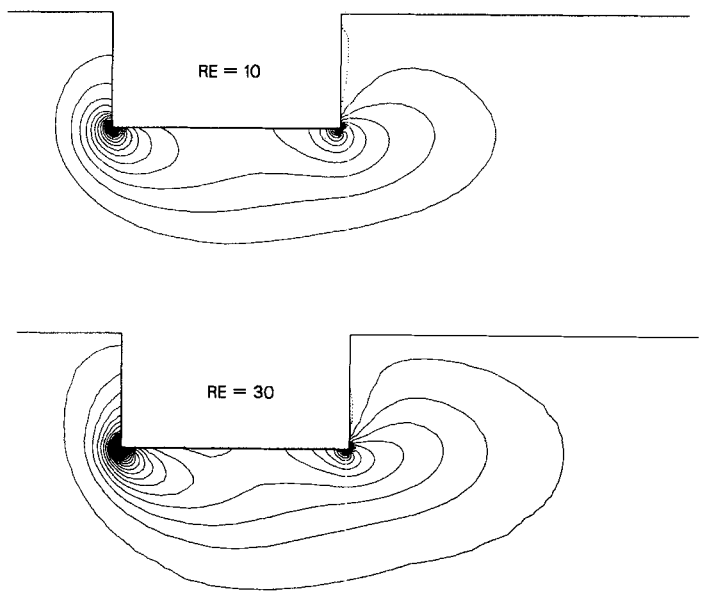

Fig. 8(a–b)

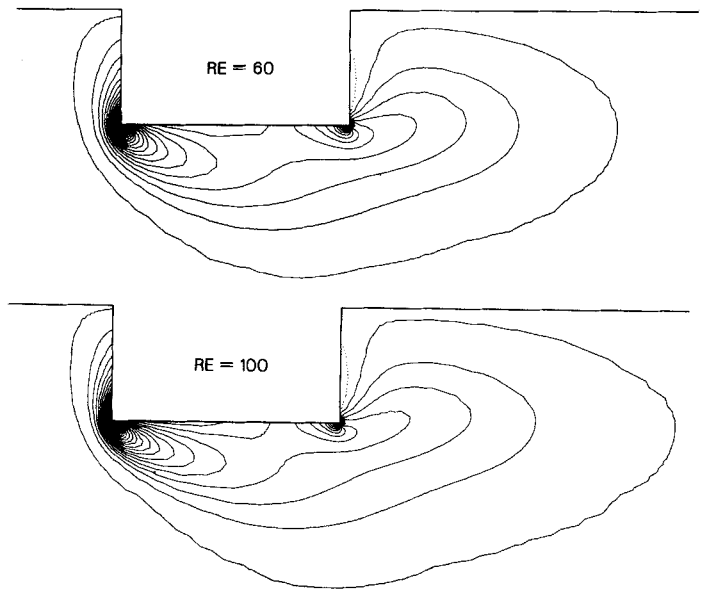

Figure 8. Contours of spanwise vorticity ω_3 in xy plane through middle of cube at Re = (a) 10, (b) 30, (c) 60 and (d) 100

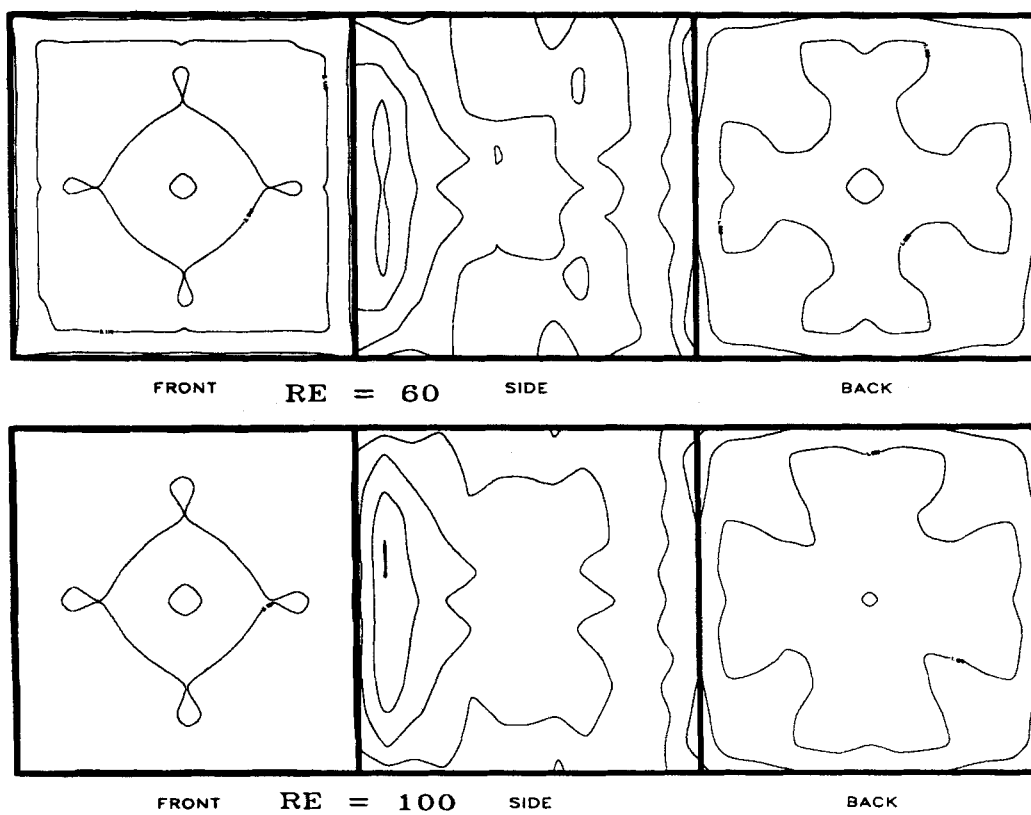

Figure 9. Contours of pressure coefficient on cube surfaces at Re = (a) 60 and (b) 100

6. CONCLUSIONS

The three-dimensional incompressible laminar flow field corresponding to a cube imbedded in a uniform stream has been computed using the vorticity–vector potential formulation of the Navier–Stokes equation. An eight-colour SOR algorithm which is well suited to the vectorization properties of the CRAY X-MP/48 supercomputer was used to solve the implicit finite difference equations. The predicted drag agreed well with experimental data, including that obtained specifically for the present study in a cube drop experiment. Other characteristics of the computed solution were in accord with those expected for similar bluff body flow fields. In future studies turbulence effects will be included as the flow at high Reynolds number is investigated.

ACKNOWLEDGEMENTS

This research was supported in part by a grant from the Ford Motor Company. Computer time was provided in full by the San Diego Supercomputer Center.

REFERENCES

1. A. K. Wong and J. A. Reizes, 'An effective vorticity–vector potential formulation for the numerical solution of three-dimensional duct flow problem', *J. Comput. Phys.*, **55**, 98–114 (1984).
2. O. R. Tutty, 'On vector potential–vorticity methods for incompressible flow problems', *J. Comput. Phys.*, **64**, 368–379 (1986).
3. A. Lin, G. De Vahl Davis, E. Leonardi and J. A. Reizes, *Proc. Ninth Int. Conf. on Numerical Methods in Fluid Dynamics*, Springer-Verlag, **218**, 380–387 (1985).
4. P. S. Bernard, 'Computation of the turbulent flow in an internal combustion engine during compression', *ASME J. Fluids Eng.*, **103**, 75–81 (1981).
5. P. S. Bernard and B. S. Berger, 'A method for computing three-dimensional turbulent flows', *SIAM J. Appl. Math.*, **42**, 453–470 (1982).
6. K. Aziz and J. D. Hellums, 'Numerical solution of three-dimensional equations of motion for laminar natural convection', *Phys. Fluids*, **10**, 314–320 (1967).
7. G. J. Hirasaki and J. D. Hellums, 'A general formulation of the boundary conditions on the vector potential in three-dimensional hydrodynamics', *Q. Appl. Math.*, **26**, 331–342 (1968).
8. G. J. Hirasaki and J. D. Hellums, 'Boundary conditions on the vector and scalar potentials in viscous three-dimensional hydrodynamics', *Q. Appl. Math.*, **28**, 293–296 (1970).
9. S. M. Richardson and A. R. H. Cornish, 'Solution of three-dimensional incompressible flow-problems', *J. Fluid Mech.*, **82**, 309–319 (1977).
10. J. C. Wu, C. Sampath and N. L. Sankar, 'A numerical study of unsteady viscous flows around airfoils', *Unsteady Aerodynamics, AGARD-CP-227*, Ottawa, 1977.
11. A. K. Wong and J. A. Reizes, 'The vector potential in the numerical solution of three-dimensional fluid dynamics problems in multiply connected regions', *J. Comput. Phys.*, **62**, 124–142 (1986).
12. L. Morino, 'Scalar/vector potential formulation for compressible viscous unsteady flows', *NASA Report 3921*, 1985.
13. H. Yang and R. Camarero, 'An improved vorticity–potential method for three-dimensional duct flow simulations', *Int. j. numer. methods fluids*, **6**, 35–45 (1986).
14. G. K. Batchelor, *An Introduction to Fluid Dynamics*, Cambridge University Press, 1967, Section 2.9.
15. W. A. Smith, *Elementary Numerical Analysis*, Reston Book, Prentice-Hall, Inc., 1986.
16. R. Raul, 'A numerical investigation of laminar and turbulent flow past a cube', *Ph.D. Thesis*, University of Maryland, 1989.
17. S. F. Hoerner, *Fluid Dynamic Drag*, Section 3, Published by the Author, Brick Town, N.J. 1965.
18. S. I. Cheng, 'Accuracy of difference formulation of Navier–Stokes equations', *Phys. Fluids*, **12**, II–34 (1969).
19. P. J. Roache, *Computational Fluid Dynamics*, Hermosa Press, 1972, Section III-C-7.
20. F. M. White, *Viscous Fluid Flow*, McGraw-Hill, 1974, Section 3, p. 226.